CHEMISTRY
A EUROPEAN JOURNAL

DOI: 10.1002/chem.200701023

Decrypting the TEM Images for Deciphering the Microstructural Code of Complex Oxides

Maryvonne Hervieu,* Christine Martin, Olivier Pérez, Richard Retoux, and Sylvie Malo[a]

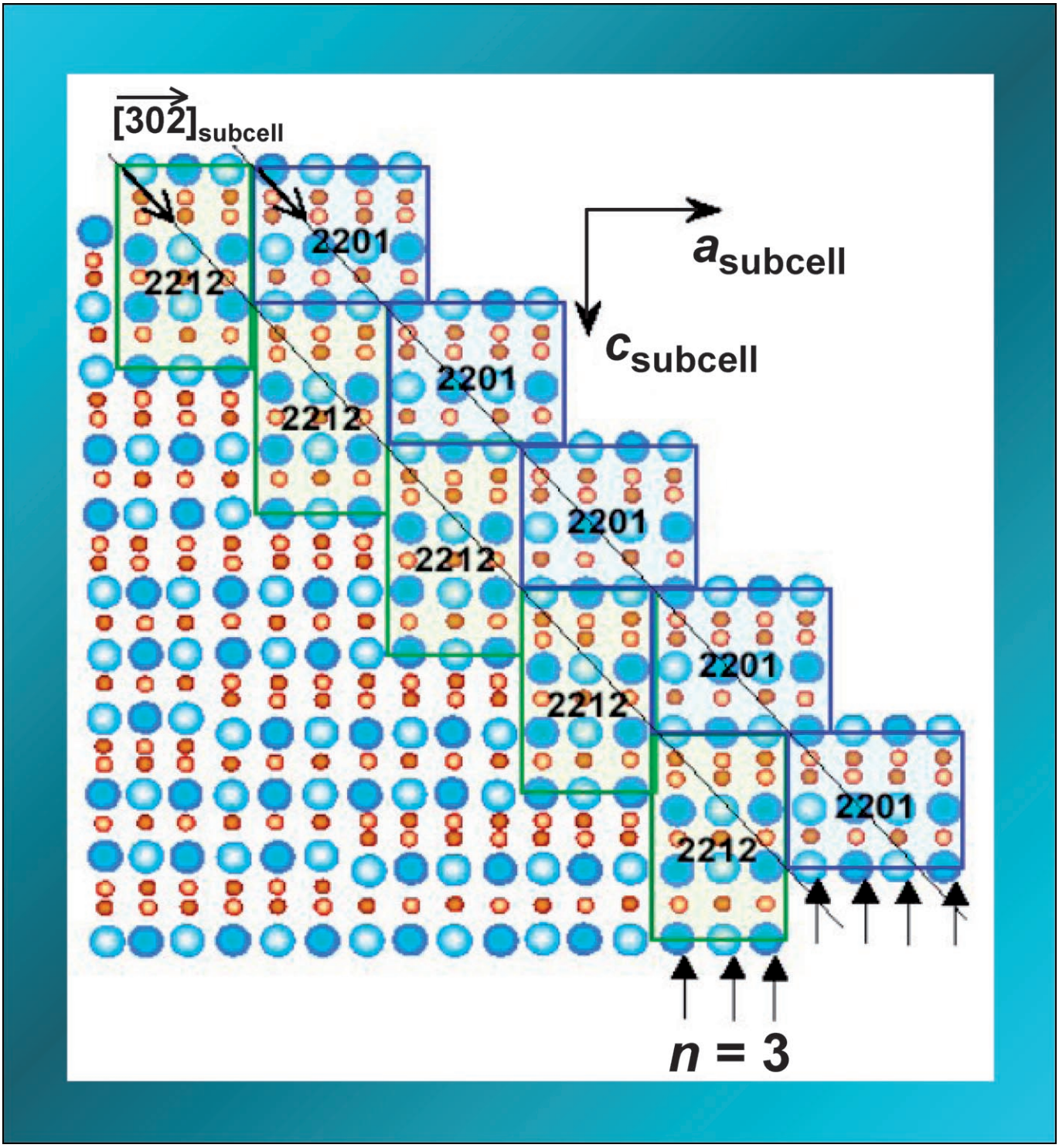

Abstract: The knowledge of the structure of the real solids is required for achieving the desired architectures in the research of new materials and/or optimizing the relationships between structure and properties. Understanding complex oxides needs accurate characterization at different length scales and the combined application of all solid-state techniques. Deciphering the relationships between all this information provides codes that allow the identification of the different structural levels, their roles and the way they interact. These step-by-step routes are illustrated through two basic mechanisms of solid-state chemistry: to determine the building units of one complex oxide in order to predict the existence of other arrangements on the one hand and to correlate complex ordering phenomena, such as those involving charges, orbitals and spins of manganese atoms in perovskite-type manganites on the other hand.

Keywords: metal oxides · nanostructures · transmission electron microscopy · X-ray diffraction

Introduction

Solid-state chemistry, in addition to the basic factors of molecular chemistry, is strongly concerned with the properties that their solidness induces. In a schooling model, the first description is an average structure, necessarily three-dimensional (3D). Afterwards, different types of departure from perfect 3D periodicity associated to the "normal" crystalline solids are accounted to understand the structural mechanisms and properties. In fact, complex materials are characterized by several successive structural levels, strongly interdependent. Knowledge of the detailed structure of the real solids requires accurate characterizations at different length scales; this is one of the keys to achieve desired architectures and/or to optimize the material properties.

Discovering new materials and tuning their properties is clearly a multistep route. No one needs to be convinced of the value of X-ray and neutron diffraction investigations. The situation is different for transmission electron microscopy (TEM), because only one high-resolution electron microscopy (HREM) image is selected among numerous through focus series. In a simplifying goal, the image contrast is often chosen to present a direct correlation between the dots and the atomic positions. The eyes of the reader catch the image and quickly associate it with the projected structure, giving one a sensation of easy interpretation. In fact, TEM studies must not be restricted to this academic use. The electron microscope is a multifunctional, multiscale tool (for the basics of TEM, see specialized books such as those given in references [1–4]). In the present paper, we present two examples of the possibilities provided by the synergy of TEM, beam diffraction techniques and magneto-transport properties to characterize different structural levels of complex oxides and investigate their associated properties.

These step-by-step routes are illustrated by two types of different studies that are of interest to the solid state chemist. In the first example, the average structure was known but the real structure unsolved. The electron diffraction (ED) and HREM studies allowed the structural mechanisms to be deciphered and the route to the characterization of a large family of complex ferrites to be opened. The second example concerns a more classical family of distorted perovskites, exhibiting complex magneto-transport properties associated to complex orderings, which involve charges, orbitals and spins of manganese atoms.

[a] Prof. M. Hervieu, Dr. C. Martin, Dr. O. Pérez, Dr. R. Retoux, Dr. S. Malo
CRISMAT laboratory, ENSICAEN
boulevard Maréchal Juin, 14050 CAEN cedex (France)
Fax: (+33) 2-31-95-16-00
E-mail: maryvonne.hervieu@ensicaen.fr

Structural Mechanisms of the Complex $Sr_4Fe_6O_{13-\delta}$-Related Oxides

The ability of iron to adopt different valence states and coordination numbers has been known for a long time to be the source of a highly rich chemistry and to generate complex structures. In the Sr-Fe-O system, iron atoms adopt the IV, V and VI coordination in the perovskite-related structures $SrFeO_{3-\delta}$[5–7] and a similar behaviour is observed in the layered Ruddlesden Popper (RP)-type phases $Sr_2FeO_{4-\delta}$[8] and $Sr_3Fe_2O_{6-\delta}$,[9] which are built up from the intergrowth of one rock salt (RS)-type and one perovskite-type layers. Note that these two last compounds are labelled 0201- and 0212-type, respectively, adopting the notation of the superconducting cuprates and related compounds.[10] Complex coordination polyhedra have been also reported for one iron-rich oxide of the Sr-Fe-O system, $Sr_4Fe_6O_{13}$, the average structure of which has been described by the alternation of perovskite-type "$Sr_2Fe_2O_5$" slabs with "Fe_2O_3" layers.[11] However, its accurate structural refinement cannot be performed due to the high complexity of the structure. Despite extensively studied ten years ago for their mixed-conducting behaviour[12–14] and thermoelectric power,[15] the origin of the complexity of these oxides was not discovered before TEM studies.[16–17]

The first level—the $Sr_4Fe_6O_{13}$-related structures are modulated: The first step was achieved thanks to electron diffraction (ED) studies,[16,17] which revealed the existence of modulated structures, as illustrated in Figure 1. The intense reflections of the [010] ED pattern are those of an *Fmmm*-type sub-cell, with $a \approx b \approx a_p\sqrt{2}$ (a_p is the parameter of a perovskite unit cell) and $c \approx 19$ Å, compatible with the average

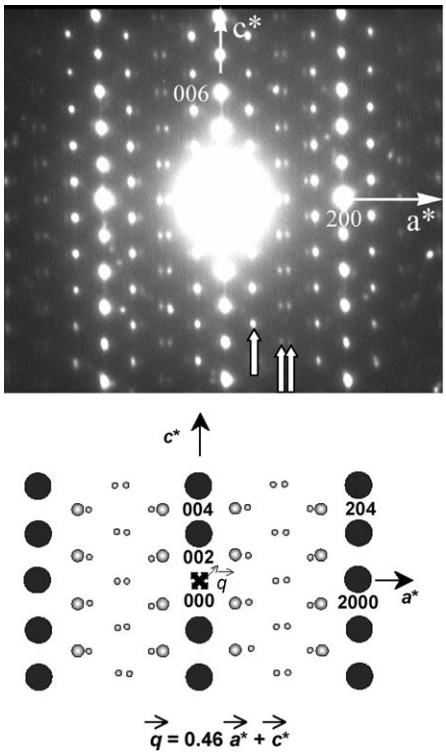

Figure 1. Top: experimental [010] ED pattern of the modulated structure of $Sr_4Fe_6O_{13-\delta}$. Bottom: schematic representation of the two sets of reflections (Bragg reflections of the sub-cell are black spots and satellites the smaller grey ones).

structural model.[11] However, a set of rather intense additional reflections is also visible (as indicated by the vertical white arrows). Both sets are schematically drawn in Figure 1 (bottom); the positions of the extra reflections induce a modulation vector $\vec{q}=p\vec{a}^*+r\vec{c}^*$, with $p=0.46$ and $r=1$. As the p component is irrational, the structure of $Sr_4Fe_6O_{13-\delta}$ can be described as an incommensurate modulated structure. The incommensurate (or "high-order" commensurate) periods of these modulated structures imply necessarily complex orders. Their origins may be a charge density wave and/or a periodic lattice distortion associated to a variation of the oxygen content, for which HREM observations would provide precious information.

No signature of the complexity is detected in the [100] HREM images (Figure 2, left); one of the characteristic contrasts consists in rows of brighter dots, correlated to the [SrO] layers, alternately spaced at 5.6 and 3.8 Å along $\vec{c}$. They are separated by rows of less grey dots associated to the different iron layers. Such images belong to the category of those, which can be intuitively interpreted in terms of projected structure, as classically observed in studies devoted to the RP's phases and derivatives.[10] They confirm that the layers stacking mode along $\vec{c}$ is -[FeO_2][SrO][FeO]-[FeO][SrO]-.

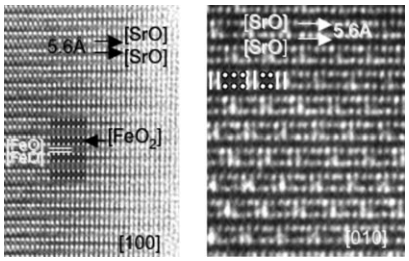

Figure 2. [100] (left) and [010] (right) HREM images (the contrast of the experimental modulated image is schematically represented by sticks and dots).

By viewing the structure along [010], the image contrasts are more complex (Figure 2, right). The intense brightness variations are the signatures of the modulation and the images show that they appear at the level of the [SrO]-[FeO][FeO][SrO] layers. To make the decryption of the contrast easier, we used a schematic representation that reproduces its experimental variation. It consists of two perpendicular white sticks that alternate with two horizontal groups of two white dots, or two horizontal groups of three white dots, in a random sequence in agreement with the irrational component p. This scheme has been superposed onto the experimental image in Figure 2. The following step consists of correlating these "dots" and "sticks" observed in the HREM images to the structural units, that is, iron polyhedra, forming the double [FeO][FeO] layer.

The oxygen content $(13-\delta)$ of the phases "$Sr_4Fe_6O_{13-\delta}$" can be varied through the synthesis processes. The first piece of information deals with the different ED studies which evidenced that the component (p) of the modulation vector along $\vec{a}^*$ varies in the range 0.5–0.4 and follows the oxygen stoichiometry according to $p=(1-\delta)/2$. More information can be obtained from the corresponding [010] HREM images, which show that whatever δ, two white "sticks" always separate groups of "two" or "three" white dots; the only variation is that the number of "three" white dots increases as p decreases, that is, as the oxygen content decreases. At this stage of the work, it clearly appeared that the origin of the structural complexity is directly associated to the oxygen stoichiometry. The contrast variation confirmed that the event arises at the level of the double [FeO]-[FeO] layers and therefore that it could be correlated with the number of $(1-\delta)/2$ oxygen atoms located in between them. The HREM images allowed the first structural models for the incommensurate modulated phases to be proposed.

Such images are indeed valuable for determining the origin of the non-stoichiometry mechanism, but they cannot provide an unambiguous answer to the exact nature of the iron atom environments. For this it is essential to simulate HREM images and to obtain the complete theoretical focus series.[4] These calculations are essential to propose an accurate interpretation of the possible variations of the contrast and to go more deeply in the different structural levels.

The second level—determination of the building units in the double iron layer: The nature of the iron polyhedra was refined, from single-crystal data, by using a 4D formalism.[18] The as-determined geometry of the iron polyhedra, their re-

spective positions and arrangement are fundamentally different from those previously proposed in the average structure.[11] The first important points are the existence of three types of iron environment, namely trigonal bipyramids (TBP), tetragonal pyramids (TP) and monocapped tetrahedra (MT). Second, it was shown that their sequences along $\vec{a}$ vary and are directly associated with the oxygen content. The $Sr_4Fe_6O_{13-\delta}$ structure is then built up from three structural units:

- The double block of trigonal bipyramids, ([TBP↑]-[TBP↓]); opposite arrows symbolizing their orientation.
- The double block of tetragonal pyramids, ([TP][TP]).
- The triple mixed block of monocaped tetrahedra, sandwiching one tetragonal pyramid, ([MT][TP][MT]).

To drawing [010] projected models of these different structural units in an incommensurate modulated structure and calculating simulated images it is necessary to use approximants. Figure 3 presents the approximant "$10a_p\sqrt{2}$", which corresponds to a sequence of 21 polyhedra in the double iron layer. The double block of trigonal bipyramids, [TBP↑][TBP↓], is generated by the presence of one extra oxygen atom (as indicated by the vertical arrows) and associated to the formation of concave zones in the rock salt slab. It clearly plays a special role, since it is formed once every two blocks, whatever the nature of the adjacent blocks: either double ([TP][TP]) block or triple ([MT][TP][MT]) block. Thanks to this accurate structure, the theoretical HREM images were calculated, using the 3D positional parameters of the approximant. We obtained the code: the two perpendicular white sticks are associated to the [TBP↑]-[TBP↓] blocks, the two horizontal groups of two white dots to the [TP][TP] blocks and the two horizontal groups of three white dots to the [MT][TP][MT].

Thus being able to interpret the HREM images, we then had the key to the third level, that is, the structural mechanism of the modulated $Sr_4Fe_6O_{13-\delta}$ phases.

The third level—the structural mechanism of the modulated $Sr_4Fe_6O_{13-\delta}$ phases: The peculiar composition $Sr_4Fe_6O_{13}$ (never obtained in our conditions of synthesis) corresponds to $\delta = 0$ and is the higher limit $p = 0.5$ value, which implies a commensurate structure; the sequence of polyhedra would be only built up from two types of blocks ([TP][TP])-([TBP↑][TBP↓]). Decreasing the oxygen content ($O_{13-\delta}$) amounts to spreading out the extra oxygen atoms of the double iron layers. Keeping in mind that one extra oxygen atom, located in between two [FeO] layers, is only located in one block ([TBP↑][TBP↓]), it amounts to the replacement of the other block of two polyhedra ([TP][TP]) by, at least, one block of three polyhedra. This structural mechanism induces the lower limit structure, which would correspond to the maximum of triple blocks according to the sequence ([TBP↑][TBP↓])([MT][TP][MT]). Such a sequence involves another commensurate structure leading to $\delta = 0.2$ ($Sr_4Fe_6O_{12.8}$) and $p = 0.4$. According to this model, an extension of the structural mechanism by increasing δ would involve the existence of new types of block, as will be shown later.[19]

The structure of $Sr_4Fe_6O_{13-\delta}$ can be now described by the stacking of two complex slices. The first one is a $[SrFeO_3]_8$ perovskite single slice built up from one $[FeO_2]_8$ layer sandwiched between two $[SrO]_8$ layers ("A" slab in Figure 3). The second is a triple rock-salt-type slice $[SrFe_2O_{3.5-\delta/2}]$ slab built up from a double iron $[Fe_2O_{2.5-\delta/2}]_8$ layer sandwiched between the two $[SrO]_8$ layers, ("B" slab in Figure 3). Retaining this simple model of one perovskite- and three rock-salt-type layers intergrown along $\vec{c}$ shows that these compounds belong to the "2201" family, according to the notation previously adopted for the $Bi_2(Sr_2)MO_{6+x}$ cuprates and related compounds.[10] As a consequence, the developed formulation $Fe_2(Sr_2)FeO_{6.5-0.5\delta}$ allows the 2201 character of the $Sr_4Fe_6O_{13-\delta}$ structure to be outlined.

This analysis of $Sr_4Fe_6O_{13-\delta}$ in terms of 2201-type structure gave another key to head towards new ferrites, the fourth level dealing with the stabilization of 2212-type members.

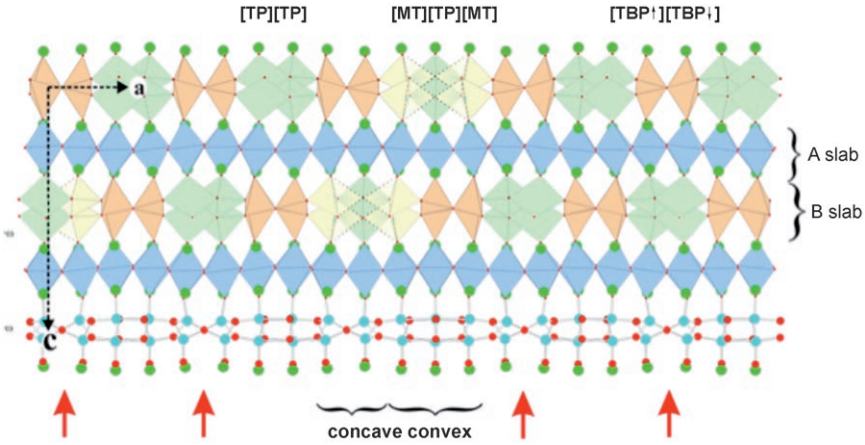

Figure 3. the two types of slabs (A = perovskite-type and B = triple rock-salt-type) as well as the three building units of the double iron layer are indicated on the top of the projection. The concave and convex zones of the rock salt slab are drawn.[18]

The fourth level—the 2212-type "iron-rich" phases: Besides the layer stacking mode, the $Fe_2(Sr_2)FeO_{6.5-0.5\delta}$ phases deserve to be compared to the other 2201 related oxides $Bi_2(Sr_2)MO_{6+x}$ (especially M = Fe[10]) with respect to their modulated character and the existence of convex/concave zones (Figure 3). The main difference between the two families is indeed the nature of the cations located in their medium rock-salt-type layers (double iron compared to double bismuth layers), but we

applied the structural mechanisms learnt from the 2201 related phases, looking especially for the possible existence of other members of a new family. A "2212" member would be formed by adding one "A′MO_3" perovskite layer for a theoretical composition $Bi_2(Sr_2)A'Fe_2O_{9\pm x}$.[20–21] In the present family, one "$SrFe^{4+}O_3$" perovskite layer requires extra oxygen that can be supplied by introducing a small amount of Bi. According to the formulation $Fe_2(Bi_xSr_{3-x})Fe_2O_{9.5-0.5\delta}$, a new phase has been successfully synthesized;[22] the c parameter of its cell is close to 26 Å, consistent with the insertion of one extra perovskite layer.

The "classic" [100] HREM images can be intuitively interpreted in terms of intergrowth of three rock-salt and two perovskite layers (the Sr positions are indicated by black arrows in Figure 4) and confirm the 2212-type structure. It is

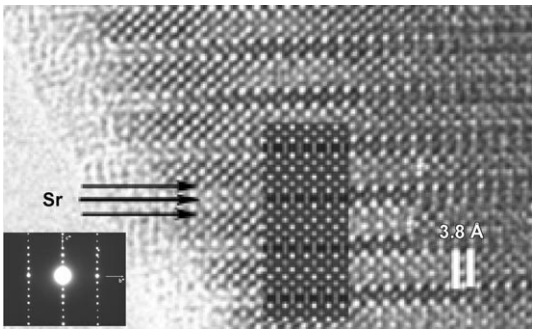

Figure 4. $Fe_2(Bi_{0.7}Sr_{2.3})Fe_2O_{9.5\pm0.5\delta}$[100] : ED pattern and HREM image.

built up from the intergrowth sequence of one block of three rock salt layers $[(Bi,Sr)Fe_2O_{3.5\pm0.5\delta}]_\infty$ with one double perovskite layer. For $Fe_2(Bi_{0.7}Sr_{2.3})Fe_2O_{9.5\pm0.5\delta}$, the ED patterns evidenced a commensurate modulation with a two-component modulation vector $\vec{q}=p\vec{a}^*+r\vec{c}^*$, p and r values being equal to 1/3 and 1, respectively (Figure 5, top). As p becomes <0.4, it means that at least one sequence of four neighbouring iron polyhedra exists between two [TBP↑][TBP↓] units. Consequently, the previous three building units of the construction set become necessarily insufficient for describing the new system. The contrast of the [010] HREM images (Figure 5, bottom) reveals that one block of two polyhedra (in the form of two sticks) alternates with one block of four polyhedra (in the form of four dots). The accurate structure of $Fe_2(Bi_{0.7}Sr_{2.3})Fe_2O_{9.5-0.5\delta}$ (Figure 6) has been determined by single-crystal X-ray diffraction. The double block ([TBP↑][TBP↓]) observed in the 2201 structure is retained on both sides of the bridging oxygen atom. The second building unit consists of one ribbon of mixed polyhedra [MT][TP][TP][MT] (Figure 7). The calculated images fit with the experimental ones, thanks to the determination of the nature of the iron atom environments.

The following steps are the characterization of the higher m members of this new structural family obeying the general formulation $Fe_2(Bi_xSr_{2-x})Sr_{m-1}Fe_mO_{9.5\pm\delta/2}$. However, other routes were opened for the tailoring of new architectures,

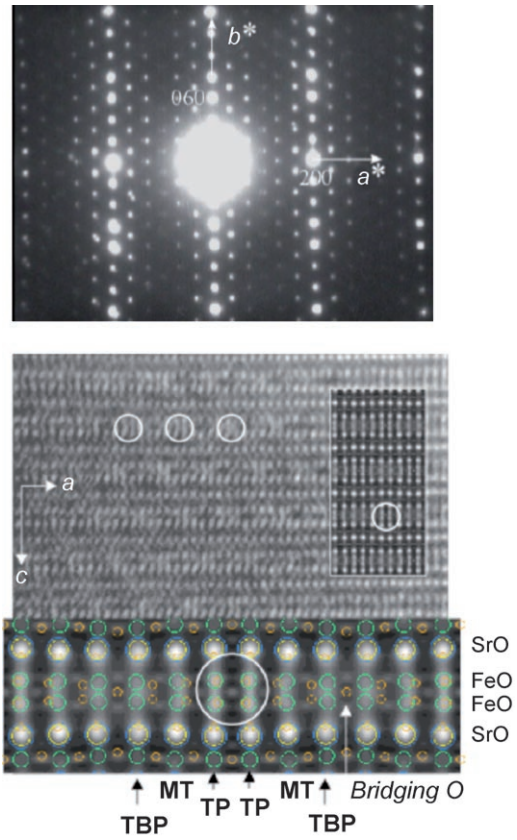

Figure 5. $Fe_2(Bi_{0.7}Sr_{2.3})Fe_2O_{9.5\pm0.5\delta}$, viewed along [010] : ED pattern (top) and experimental HREM image (bottom), the calculated image is superposed and the projected structure enlarged.

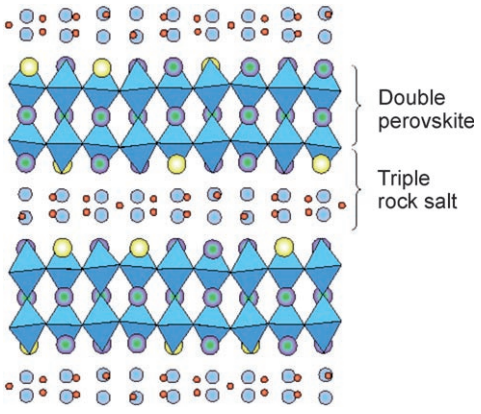

Figure 6. $Fe_2(Bi_{0.7}Sr_{2.3})Fe_2O_{9.5\pm0.5\delta}$: projection along [010].

Figure 7. The four building units forming the double iron layers of the 2201- and 2212-type structures.

based on different structural mechanisms, such as the possible formation of shear planes.

The fifth level—formation of shear structures: The structural phenomenon called crystallographic shear, reported in the rutile-type oxides[23] M_nO_{2n-1}, can be described by a periodic motif resulting from the translation of two parts of one parent crystal structure with respect to each other, the plane separating the two parts being called the crystallographic shear plane (CSP). The formation of CSPs has been also reported in the complex cuprates and ferrites systems,[24] forming shear structures (also called terrace-like structures); for example, $Bi_6Ba_4Cu_2O_{15}$, which is related to the 2201-type structure and the Bi-Sr-Cu oxycarbonates $Bi_{15}Sr_{29}Cu_{12}(CO_3)_7O_{56}$.[25] Similar mechanisms were also observed in the Bi-rich ferrites with terrace structures related to the 2201-[26] and 2212-type structure $Bi_{12}Sr_{18}Fe_{10}O_{52}$.[27–29] Considering the general rules of the formation of shear structures, the divalent Pb^{2+} was a good candidate to generate shear structures in the iron-rich 2201- and 2212-type structures described above, due to its size, divalent character and possible role of the $6s^2$ lone pair. The research was fruitful, several original phases being observed, as exemplified for the composition $Pb_4Sr_{13}Fe_{24}O_{53}$.

In a first approach, the [010] ED patterns (inserted in Figure 8 top) exhibit similarities with those of the 2201- and 2212-type structures, with the presence of intense reflections associated to the sub-cell and satellites. The modulation vector $\vec{q}^* = p\vec{a}^* + r\vec{c}^*$ lies along the [203]* direction of the sub-cell, with an amplitude $1/17(2\vec{a}^* + 3\vec{c}^*)$. The associated super-cell is monoclinic and its parameters refined from the powder X-ray diffraction data have been refined to $a_T = 35.039(2)$ Å, $b_T = 5.5897(2)$ Å, $c_T = 25.662(2)$ Å and $\beta = 98°102(2)$, space group *Cc* or *C*2/*c* (the T index refers to a "terrace" structure).

Based on the image contrasts of the 2201- and 2212-type structures, the HREM images gave the solution for the structural-type of this novel phase. In Figure 8, the rows of bright dots are associated to the [(Sr,Pb)O] layers and the grey ones to the iron layers: along the [100] direction, a contrast similar to the one observed for the 2201- and 2212-type members is observed, but only over a few octahedra. In contrast to the parent structures, the double bright and grey dots are not regularly stacked along $\vec{c}$, but suffer translations, according to the mechanisms observed in the terrace-like structures. In that way, they form two types of ribbons parallel to the $[302]_{sub}$ direction. A model has been deduced from HREM images: one observes two types of ribbons parallel to the $\overrightarrow{302}_{sub}$ direction (the $\vec{a}$ and $\vec{c}$ axes of the sub-cell are given Figure 8, bottom). One ribbon is made of 2212-type bricks ($3/2\vec{a}_{sub}$ wide), and the second is made of 2201-type bricks ($2\vec{a}_{sub}$ wide). The new structure[30] is therefore described as the intergrowth of 2201-type slices, *m* octahedra large, and 2212-type slices, *n* octahedra large, that is, belonging to a complex family of terrace structures $[Fe_2(Sr_2)FeO_{6+\varepsilon}]_m^{2201}[Fe_2(Sr_{3-x}Pb_x^{2+})Fe_2O_{9+\varepsilon}]_n^{2212}$; in the present case, $m = 4$ and $n = 3$.

The discovery of this phase opens the route for the research of other [*m*,*n*] members of a large family, exhibiting shear structures in the Sr-Pb-Fe-O system.

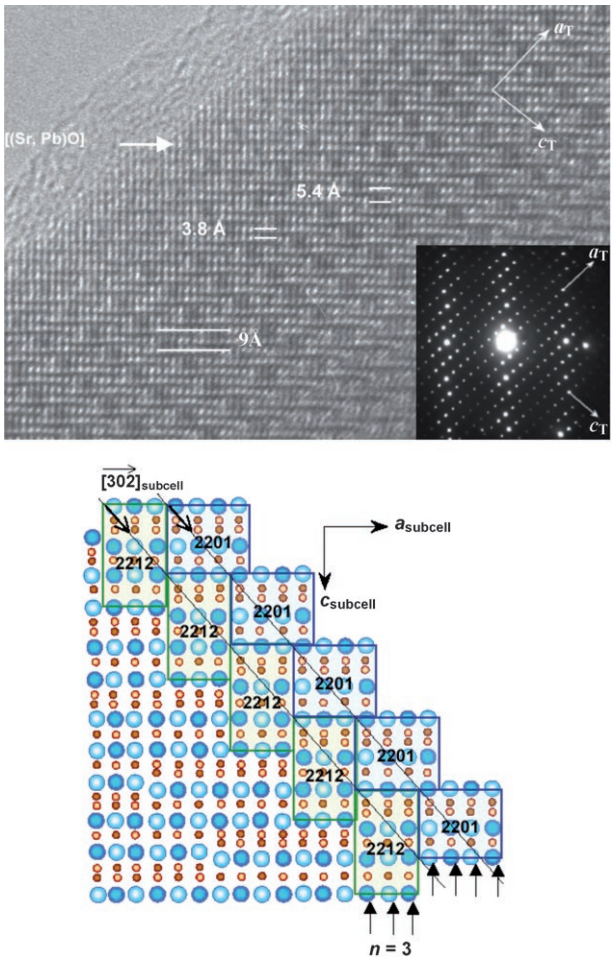

Figure 8. $Fe_2(Pb_{0.7}Sr_{2.3})Fe_2O_{9.5\pm0.5\delta}$, viewed along [010]. ED pattern and HREM image (top) and idealized drawing of the terrace structure (bottom), member $m = 4/n = 3$ of the family $[Fe_2(Sr_2)FeO_{6.5\pm0.5\delta}]_m^{220}[Fe_2(Sr_{3-x}Pb_x^{2+})Fe_2O_{9.5\pm0.5\delta}]_n^{2212}$.

Codes of the Magnetoresistant Manganites $(A_{1-x}A'_x)(Mn_{1-y}M_y)O_3$

The overwhelming majority of the recently discovered colossal magnetoresistant[1] (CMR) manganites have a perovskite structure given by the general formula $(A_{1-x}A'_x)MnO_{3-\delta}$. Numerous physical and chemical parameters could influence their magneto-transport properties; as an example, they are strongly dependent on the cationic composition through (A,A′,*x*) and the exact oxygen content. These changing properties are intimately associated to structural and microstructural changes, since the perovskite structure has many degrees of freedom. Most of them adopt the cubic structure with a *Pm3m* symmetry at high enough temperature. At lower temperatures, structural modifications or distortions from the ideal perovskite generate structures with a lower symmetry,[31] derived from the cubic structure by tilting and/or deformation of the MnO_6 octahedra. As commonly ob-

[1] A. Fert and P Grünberg were awarded the 2007 Nobel Prize in Physics for the discovery of giant magneto resistance (GMR)

served in numerous systems, the strain energy associated with the spontaneous deformation at the unit cell level is minimised by transforming one crystal into a patchwork of oriented domains, nanometer or micrometer sized. The number of different orientation variants depends on the ratio of the order of the point groups of parent and products.[32] These domains are clearly a factor limiting the refinement accuracy of the single crystal diffraction data in numerous cases. TEM studies are then a really efficient tool in determining the microstructural state of these perovskites.

The limit manganites $La^{3+}Mn^{3+}O_3$ and $Pr^{3+}Mn^{3+}O_3$ are A-type antiferromagnets (AFMs), due to AFM super-exchange interactions. The presence of Mn^{4+} ions can be induced in the matrix by introducing alkaline earth (A^{2+}) cations; it therefore involves ferromagnetic and metallic states below the Curie temperature T_c through double-exchange mechanisms. The existence of highly complex phenomena was evidenced, which clearly show that double-exchange cannot be the sole explanation for the observed transformations. This is especially the case for $Ln_{1-x}Ca_xMnO_3$ manganites, which exhibit "charge ordering" (CO between Mn^{3+}/Mn^{4+}) and "orbital ordering" (OO) below the $T_{CO/OO}$ temperature, both being competing interactions, and "spin ordering" below T_N.[33–35] The mixed valence of manganese, the average size of the A cations, the mismatch between the Ln and Ca cations and, in a more general way, any mechanism generating disorder are considered the major parameters influencing the CMR properties. They are all directly linked to the crystal structure and the chemical bonds, and are strongly interdependent. All these effects control the hole-carrier density and the density of defects.

For understanding the codes that we aim to describe, it is important to recall that in these materials the generic terms "defects" cover different crystallographic levels from strain effects generated by the coexistence of the oriented variants (nanometer to micrometer scale) to doping effects (atomic scale).

Acquiring the codes of the parent structures $Ln_{1-x}Ca_xMnO_3$: In the first section devoted to the ferrites, our "code" challenge was to use the combination of TEM and diffraction techniques in order to understand the mechanisms and to associate the different structural units to their TEM signatures. In the case of the $Ln_{1-x}Ca_xMnO_3$ oxides, the complexity results from charge-, orbital- and spin-ordering mechanisms, which generate the varying physical properties, structures and micro- or nanostructures. The combination (X-ray and neutron diffraction techniques/magnetotransport measurements) is the only one liable to provide accurate codes for TEM studies and, in return, the last ones are likely the only ones for understanding the mechanisms at the nanometer scale.

Charge and orbital ordering ($0.3<x<0.8$): In the composition range $0.3<x<0.8$, all the manganites exhibit a *Pnma*-type perovskite structure at RT ($a\approx a_p\sqrt{2}$, $b\approx 2a_p$, $c\approx a_p\sqrt{2}$). At low temperature ($T<T_{CO}$), the structure is ordered, characterized by a doubling of the periodicity along $\vec{a}$ ($\approx 2a_p\sqrt{2}$) and a CE-type AFM (e.g.[33–34]). The information recorded by a TEM study is illustrated in Figure 9. At

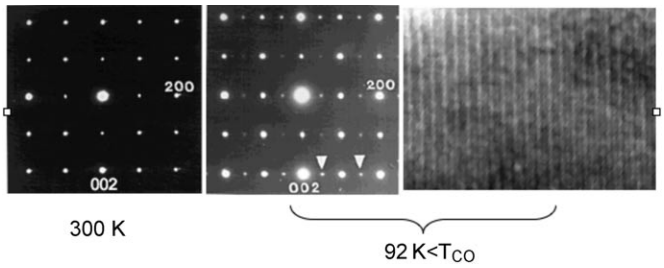

Figure 9. typical TEM information : Left: [010] ED pattern recorded at $T>T_{CO/OO}$, corresponding to a *Pnma* subcell. Middle: same crystal at $T<T_{CO/OO}$. Right: lattice image showing regularly spaced fringes at $T<T_{CO/OO}$.

$T>T_{CO}$, the [010] electron diffraction (ED) patterns are characterized by the system of intense reflections characteristic of the *Pnma* structure (Figure 9, left), whereas at $T<T_{CO}$ a set of extra reflections is observed (as indicated by small white arrows in Figure 9, middle). The satellites intensities are rather strong, in contrast to those of the corresponding peaks in the X-ray and neutron diffraction patterns. This effect, partly owed to the larger scattering factors of the atoms for electrons relative to those for X-rays, allows a rather easy observation of the components of the modulation vector. The contrast of the lattice images recorded at 92 K consists of fringes systems. One example characterized by white fringes regularly spaced by 10.9 Å $=2\sqrt{2}a_p$ is given in Figure 9 (right: $Sm_{0.5}Ca_{0.5}MnO_3$ sample). Contrary to the contrast of the HREM images, these fringes cannot be directly correlated to the atomic planes, but they give the unique opportunity to locally determine the periodicities along the modulation vector, to detect any deviation to them and also the possible existence of non-modulated zones in the crystallites. They provide, at the nanometric scale, a simple but invaluable view of the material.

The study of the charge ordering, carried out in the systems $Ln_{1-x}Ca_xMnO_3$,[36–47] showed that the behaviours of the hole- ($x<0.5$, i.e., rich in Mn^{3+}) and electron-doped manganites ($x>0.5$, i.e., rich in Mn^{4+}) are clearly different. Considering only the electron-doped domain, the ED studies versus temperature showed that, over a large composition range up to 0.78, a complex system of satellites also appear along $\vec{a}^*$. Compared with other diffraction technique data and magnetic measurements, one of advantages of this technique is the ability to follow, step-by-step and visually, the evolution of the modulation versus temperature. The complex orderings take place in three steps as illustrated in Figure 10.

Evolution versus temperature:

- At RT, in the paramagnetic state, the structure is Pnma-type and the ED patterns remain unaltered down to $T_{CO/OO}$.

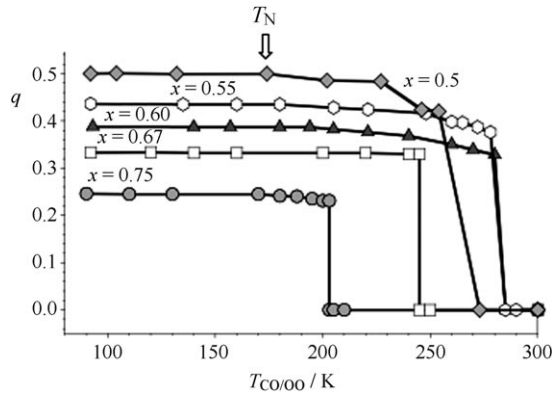

Figure 10. Variation of the amplitude of the modulation vector in the $Sm_{1-x}Ca_xMnO_3$ system ($0.5 \leq x \leq 0.75$).

- At $T_{CO/OO}$, the weak satellites appear. In this second step, associated to the so-called pinning of the modulation, the wave vector pa^* is temperature dependent, p and the intensity of the satellites increases as T decreases.
- At a lower temperature, the amplitude of the modulation vector pa^* and the intensity of the satellites remain constant, leading to a plateau in the q vs. T curves (Figure 10). In the modulated systems, the low temperature phase (the "lock-in phase") is stabilized at this temperature. In most of the Ca based compounds, this temperature coincides with the Néel temperature (T_N) determined from magnetic measurements and neutron diffraction.

Evolution versus x:For the $Sm_{1-x}Ca_xMnO_3$ system in the range $0.5 \leq x \leq 0.75$, the amplitude of the modulation vector pa^* varies with the composition, below T_N. It follows the $[Mn^{4+}/Mn^{3+}+Mn^{4+}]$ ratio and remains close to 1−x, becoming commensurate or incommensurate (Figure 10). As an example, the supercell of $Pr_{0.33}Ca_{0.67}MnO_3$ (Figure 11, left) is commensurate, with a tripling of the a parameter at 92 K and the lattice images show the high regularity of the periodicity with a system of fringes spaced by 16.5 Å ($a = 3a_p\sqrt{2}$) in Figure 11 (right). These modulations are associated to complex orderings of the Mn^{3+} and Mn^{4+} ions, of the d_{z^2} orbitals of Mn^{3+} (orbital ordering OO associated to the Jahn–Teller effect) and the appearance of the plateau to the spins ordering, fitting with the Néel temperature. Different

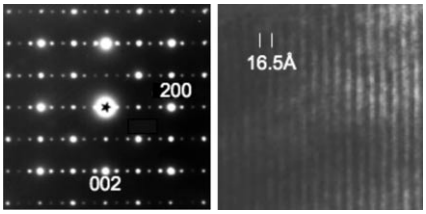

Figure 11. [010] ED pattern (left) and lattice image (right) of $Pr_{0.33}Ca_{0.67}MnO_3$.

models have been proposed for the commensurate $Ln_{0.33}Ca_{0.67}MnO_3$.[36–37] Combining TEM and neutron diffraction refinement of the nuclear and magnetic structures allows completely describing the ordering phenomena in terms of "parquet-like" (also called "multi-axes" structure by referring to the spin orientation).[37] For $Pr_{0.25}Ca_{0.75}MnO_3$, another commensurate superstructure is obtained, with $a = 4a_p\sqrt{2}$. For intermediate values of x, the compounds exhibit different incommensurate modulated structures, p varying as 1−x, that is, as the Mn^{3+} content from 0.5 to 0.75.

CMR in the $Sm_{1-x}Ca_xMnO_3$ system $0.8 \leq x \leq 0.85$: For this composition range, a different behaviour is observed. There is a strong coupling between charge carriers and spins, so that the CMR properties are strongly influenced by the strength of the CO/OO. One of the consequences is that they are highly sensitive to any event able to destabilize it. In the $Sm_{1-x}Ca_xMnO_3$ system, CMR properties are observed at one of the boundaries between two structural and magnetic domains. The magnetization of the Sm based compounds in the range $0.025 \leq x \leq 0.25$ is given in Figure 12 to

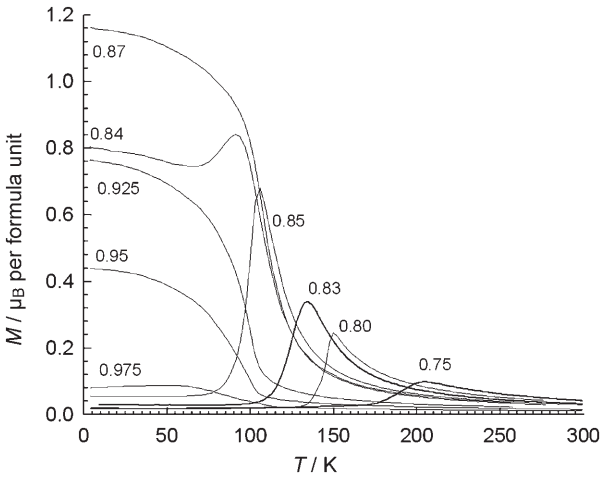

Figure 12. Ca-rich $Sm_{1-x}Ca_xMnO_3$ system : magnetization curves in the range $0.025 \leq x \leq 0.25$.

illustrate the nature of the magnetotransport information in the electron-doped manganites. The temperatures of the maxima $M(T)$ decrease with x, from 210 K for $x = 0.75$ down to 110 K for $x = 0.85$,[33] whereas their M values increase simultaneously. The behaviour of $Sm_{0.15}Ca_{0.85}MnO_3$ suggests that the CMR effect results from the strong competition between FM and AFM interaction systems.

Despite the fact that these magnetization curves exhibit an apparent continuous evolution in the range $0.75 \leq x \leq 0.975$, the ED investigation evidenced a different low-temperature structure. As mentioned above, the $x = 0.75$ manganite is a charge ordered phase, with a $4a_p\sqrt{2}$ superstructure. On the opposite, no signature of CO can be detected in the $x = 0.85$ manganite, but a strong monoclinic distortion ($P2/m$ space group) of the *Pnma* subcell is observed (Figure 13, left). In the [010] ED patterns, this distortion

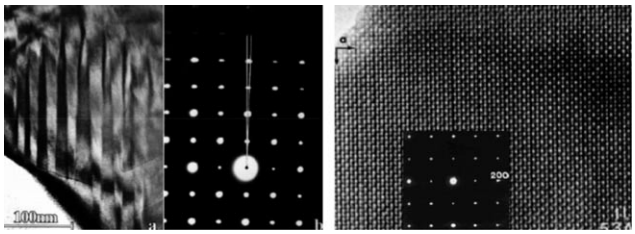

Figure 13. $Sm_{0.15}Ca_{0.85}MnO_3$: Left: [010] bright field image and ED pattern which are the signature of a monoclinic distortion at $T < T_{CO/OO}$. Right: highly regular HREM image at RT ($T > T_{CO/OO}$).

generates a typical splitting of the reflections (see the two white lines in Figure 13, right). Another signature is the formation of twinning domains, which are easily identified by TEM studies: in the bright field images, the twinning domains can be imaged by alternating dark and less dark stripes, a few ten nanometers wide (Figure 13, left). Such a distortion, from the orthorhombic cell (PM state) to the monoclinic cell (AFM state), induces strong strain effects, which are released by the formation of twinning domains. In this part of the system, before drawing a correlation between the magnetic and structural states, it was important to systematically carry out a study in the paramagnetic state to detect the existence of any ordering or any other effect at the atomic level that could be associated to the lowering of the lanthanide and oxygen content. All the HREM images recorded for the different samples exhibit a regular contrast typical of the *Pnma*-type perovskite (Figure 13, right), which allows the hypothesis of short range ordering effects to be discarded.

For a compound with $x = 0.85$, the structural transition orthorhombic (*Pnma*)-monoclinic (*P2/m*) is abrupt and its temperature coincides with the resistive and magnetic transitions. Neutron diffraction evidenced a C-type AFM structure.[28] Another point is of interest for collecting the codes. For $x = 0.8$, at the boundary between two different phases, namely the modulated charge-ordered ($x = 0.75$) and the AFM C-type structure ($x = 0.85$), an abrupt transition is also observed at 155 K. However, close to this transition temperature, the reflections are cross-shaped, with arms along $[101]_p$*; in the bright field images, a so-called "tweed structure" is observed. This tweed structure is generally associated with a pre-configuration of the monoclinic structure in different variants. It smoothly vanishes with increasing temperature.

CMR in the $Sm_{1-x}Ca_xMnO_3$ system $0.9 \le x \le 1$: In the domain $0.9 \le x < 0.975$, the *Pnma*-type structure is observed from room temperature down to 92 K, without any deviation of the orthorhombic structure; for this composition domain, the neutron diffraction study evidenced a cluster glass state associated to the formation of weak FM zones diluted in a AFM matrix. The limit $CaMnO_3$ exhibits a G-type AFM structure.

The correlation between the magnetotransport measurements, the magnetic and nuclear structures refined from neutron diffraction patterns and the TEM studies are summarized in Figure 14.

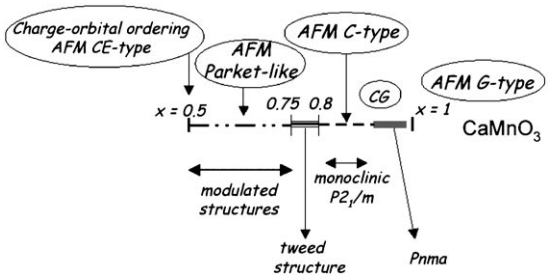

Figure 14. $Sm_{1-x}Ca_xMnO_3$ system: representation of the different nuclear and magnetic structures, as well as the nanostructures on a pseudo-diagram as a function of the Mn^{3+} content.

The code efficiency—the Mn-doped compounds: Doping the manganese sites of $Pr_{0.5}Ca_{0.5}MnO_3$ with a magnetic cation in the absence of magnetic field was shown to induce CMR properties of $Pr_{0.5}Ca_{0.5}Mn_{1-y}Cr_yO_3$, as a result of the competition between the FM metallic and AFM insulating domains.[48–52] Three important parameters govern these mechanisms, identified through several structural and microstructural studies of the $Ln_{0.5}Ca_{0.5}Mn_{1-y}M_yO_3$ compounds:

1) An impurity effect, which could induce a pinning of the discommensurations.
2) A charge effect, which results from the possible modifications of the Mn^{3+}/Mn^{4+} ratio depending on the oxidation state of M.
3) A magnetic effect induced by the possible FM or AFM alignment of the spins of the magnetic M cations with regard to those of the Mn.

For example, doping $Sm_{0.2}Ca_{0.8}MnO_3$ by Ru induces an original metal-to-metal transition, a spectacular increase of T_c up to 240 K and CMR effect.[53] From the charge-balance mechanism, introducing Ru^{5+} would induce an increase of the Mn^{3+} content: $y = 0.08$ Ru^{5+} increases the Mn^{3+} content from 0.2 to 0.28 (Table 1).

As previously mentioned, one of the research axes was to weaken CO/OO in the hope to generate CMR, FM and also, metallic properties by using different processes. The studies carried out in the $Ln_{0.5}Ca_{0.5}Mn_{1-y}M'_yO_3$ systems currently lead us to conclude that replacing manganese by a

Table 1. Developed formulations of $Ln_{1-x}Ca_xMn_{1-y}M_yO_3$ manganites.

$x = 0.8$	$x = 1$
$Sm_{0.2}Ca_{0.8}(Mn^{3+})_{0.2}(Mn^{4+})_{0.8}O_3$	$Ca(Mn^{3+})_0(Mn^{4+})_1O_3$
$Sm_{0.2}Ca_{0.8}(Mn^{3+})_{0.28}(Mn^{4+})_{0.64}(Ru^{5+})_{0.08}O_3$	$Ca(Mn^{3+})_{0.28}(Mn^{4+})_{0.58}(Mo^{6+})_{0.14}O_3$

foreign cation, whatever the charge and the magnetic state, induces disorder on the Mn sites and consequently hinders CO/OO to develop, up to its destruction.

Keeping in mind this charge-balance mechanism, the action of high valence cations, such as Mo^{6+} and W^{6+}, was expected to be more efficient. Applied to the limit compound $CaMn^{4+}O_3$ (AFM G-type), it should quickly increase the Mn^{3+} content (Table 1) and quickly modify its properties.

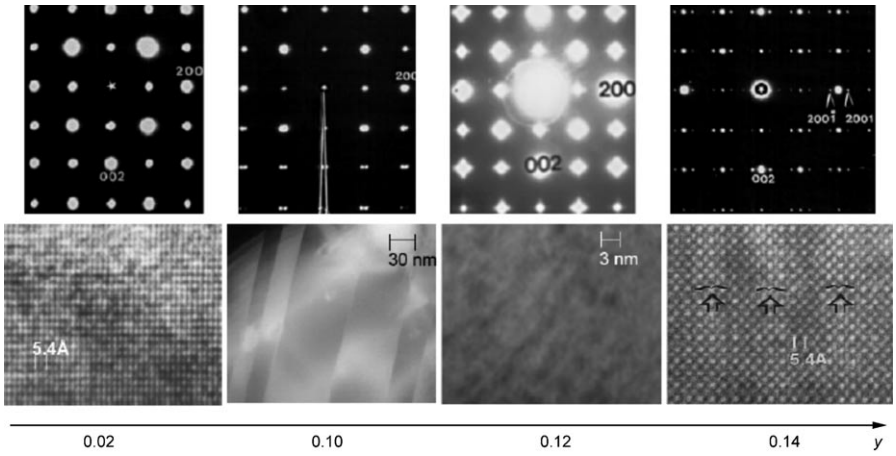

Figure 15. [010] ED patterns (top) and typical images (bottom) of the $CaMn_{1-y}M'_yO_3$ compounds, in their low temperature forms versus y.

Study of $CaMn_{1-x}M_xO_3$ (M = Mo, W):[54–57] The solid solution $CaMn_{1-y}M'_yO_3$ ($M = Mo^{6+}$ and W^{6+}) is stabilized up to $y = 0.15$. All the ED patterns of the paramagnetic forms exhibit the orthorhombic *Pnma*-type perovskite and the HREM images confirm that Mo and W species are randomly distributed over the Mn sites of the matrix.

Typical ED patterns and images of the low-temperature forms are given versus the doping content in Figure 15 according to the sequence: $y = 0.02$, 0.10, 0.12 and 0.14. Note that the scales of the four selected images are very different: they are of a few Å for $y = 0.02$ and 0.14, to a few tens Å for $y = 0.12$ and lastly up to a few tens nanometers for $y = 0.10$. This emphasizes the necessity to have a multiscale view of the materials.

- In the range $y = 0$–0.05: the ED pattern is that of a *Pnma* structure. The contrast at low temperature is more regular than that at RT, in agreement with the unchanged *Pnma*-type distortion of the perovskite cell.
- In the range 0.06–0.12: the splitting of the reflections and the formation of twinning domains are characteristic of a distorted monoclinic cell ($P2_1/m$).
- For $y \approx 0.12$: the ED patterns exhibit elongated spots. The corresponding image shows a tweed structure, characteristic of a phase transition, suggesting that this composition is at the borderline between two different low-temperature structures and, consequently, two different magnetic behaviours.
- For $y > 0.12$: the intense reflections belong to the *Pnma* sub-cell and a second system of satellites is observed (signatures of a modulated structure) in incommensurate positions; the average modulation vector is $q = 0.24\,a^*$. The TEM study of $CaMn_{0.86}Mo_{0.14}O_3$ provides HREM images of the modulated structure with a local periodicity of 21.6 Å $\approx 4a_p\sqrt{2}$ (i.e. $p = 1/4$). The presence of these satellites for $CaMn_{0.86}Mo_{0.14}O_3$ calls indeed a comparison with the ones observed for the Sm and Nd-based $Ln_{1-x}Ca_xMnO_3$ compounds for values of x close to 0.75. The developed formulation could be calculated from the charge balance, $Ca(Mn^{3+})_{0.28}(Mn^{4+})_{0.58}(Mo^{6+})_{0.14}O_3$ (Table 1).

In the above section, we showed that the meticulous correlations, established between the TEM, diffraction and magnetotransport properties, provide us with efficient codes. Thanks to the fact that the different states have characteristic signatures in TEM data, the codes were extended to different $Ln_{1-x}A_xMnO_3$ systems, and can be used regardless of what Ln, A and x are. It is more remarkable to note that the code can be also applied even when the Mn sites are doped, as illustrated in Figure 14 and Table 2. The structure/nanostructure sequences at low temperature correspond extremely well. Table 2 compares the $CaMn_{1-y}Mo_yO_3$ system to the $Pr_{1-x}Ca_xMnO_3$ one, in five columns: 1) the doping element content (y); 2) the Mn^{3+} content induced by the doping y; 3) the structure-type of the low temperature form; 4) the magnetic behaviour (obtained from magnetic measurements and neutron diffraction) and 5) the composition (x value, that is, the Mn^{3+} content) of the manganite $Pr_{1-x}Ca_xMnO_3$ in which are observed similar structural and magnetic characteristics. This is also perfectly illustrated by considering, in Figure 14, the sequence of structures and mi-

Table 2. Comparison of the Mn^{3+}-poor manganites in the $CaMn_{1-y}Mo_yO_3$ and $Pr_{1-x}Ca_xMnO_3$ systems.

y range	Mn^{3+}-induced	Low T form	Magnetic behaviour	Equiv. x[a]
0–0.05	0–0.10	*Pnma*	G-type AFM small weak FM areas	0.025–0.10
0.06–0.10	0.12–0.20	$P2_1/m$	C-type AFM	0.10–0.20
0.10–0.12	0.20–0.24	tweed and SRO		0.20–0.24
0.12–0.15	0.24–0.30	modulated structure	CO/OO AFM	0.24–-

[a] For the $Pr_{1-x}Ca_xMnO_3$ system.

crostructures versus $1-y$: we find the same structural and microstructural characteristics, which allow a first efficient diagnosis on the sample state by a simple TEM experiment to be made.

Having the code through the TEM data allow understanding the complex mechanisms of these fascinating materials. Phase segregation, phase transition under electron irradiation, nanostructural differences between field-cooled and zero-field-cooled samples, or the role of pinning centres of the foreign cations are, for example, among the problems that we have investigated and solved in the domains of the manganites. It has also allowed us to understand charge-orbital ordering phenomena in Ruddlesden–Popper phases and the role of strain effects in thin films.

Conclusion

The diversity of today's advanced materials is based on the knowledge of how to attain novel structures or to improve existing materials. There are a number of possible strategies to realize material design, from an empirical to a logical approach. A basic set of models able to describe the essential features of reactivity, structures and properties is in any case the first needed key. Iono–covalent architectures have been often compared to construction sets, based on given building units, the nature of which defining the structural family and their number, the member of the family. The huge number of papers presently devoted to "classics" such as perovskites and layered oxides shows that, even in these basic compounds, the details of these structures and their relationships with physical properties remain complex. One of the strategies, presented herein is the research of "signatures", using transmission electron microscopy, of the different structural levels existing in the complex materials, at different length scales. The challenge is therefore to achieve an accurate interpretation of these signals, thanks to the combination of any of the required solid-state techniques. All the results contribute to the elucidation of the complex character of the materials. The interest of the two examples described in this paper shows that mechanisms, as various as charge- and orbital-ordering or complex blocks of iron polyhedra, can be interpreted. Following this route, we are able to decrypt TEM images and having this code, the solid-state chemist can obtain the basis for discovering novel materials and tuning their specific properties.

[1] P. B. Hirsch, *Electron Microscopy in Thin Crystals*, Krieger, New York, **1977**.
[2] S. Amelinckx, D. van Dyck, J. van Landuyt, G. van Tendeloo, *Electron Microscopy*, Wiley-VCH, Weinheim, **1997**.
[3] J. M. Cowley, *Electron Diffraction Techniques*, Oxford University Press, Oxford, **1993**.
[4] S. Amelinckx, D. van Dyck, J. van Landuyt, G. van Tendeloo, *Handbook of Microscopy*, Wiley-VCH, Weinheim, **1997**.
[5] J. C. Grenier, E. A. Norbert, M. Pouchard, P. Hagenmuller, *J. Solid State Chem.* **1985**, *58*, 243.
[6] Y. Takeda, K. Kano, T. Takada, O. Yamamoto, M. Takano, N. Nakayama, Y. Bando, *J. Solid State Chem.* **1986**, *63*, 237.
[7] M. Takano, T. Okita, N. Nakayama, Y. Bando, Y. Takeda, O. Yamamoto, J. B. Goodenough, *J. Solid State Chem.* **1988**, *73*, 140.
[8] P. Adler, *J. Solid State Chem.* **1994**, *108*, 275.
[9] F. Prado, L. Mogni, G. J. Cuello, A. Caneiro, *Solid State Ionics* **2007**, *178*, 77.
[10] "Crystal Chemistry Of High T_c superdonctucting Copper Oxides", B. Raveau, C. Michel, M. Hervieu, D. Groult, **1991**, *Springer Series in Materials Science Volume 15*, Springer, Berlin–New York, **1991**.
[11] A. Yoshiasa; K. Ueno, F. Kanamaru, H. Horiuchi, *Mater. Res. Bull.* **1986**, *21*, 175; K. Ueno, F. Kanamaru, H. Horiuchi, *Mater. Res. Bull.* **1986**, *21*, 175.
[12] B. Ma, U. Balachandran, J.-H. Park, *J. Electrochem. Soc.* **1996**, *143*, 1736.
[13] B. Ma, U. Balachandran, *Solid State Ionics* **1995**, *53*, 100.
[14] S. Kim, Y. L. Yang, R. Christoffersen, A. J. Jacobson, *Solid State Ionics* **1998**, *109*, 187.
[15] S. Gugilla, T. Armstrong, A. Manthiram, *J. Solid State Chem.* **1999**, *145*, 260.
[16] B. Mellenne, R. Retoux, C. Lepoittevin, M. Hervieu, B. Raveau, *Chem. Mater.* **2004**, *16*, 5006.
[17] M. D. Rossel, A. M. Abakumov, G. Van Tendeloo, J. A. Pardo, J. Santiso, *Chem. Mater.* **2004**, *16*, 2578.
[18] O. Pérez, B. Mellenne, R. Retoux, B. Raveau, M. Hervieu, *Solid State Sci.* **2006**, *8*, 431.
[19] D. Grebille, C. Lepoittevin, S. Malo, O. Pérez, N. Nguyen, M. Hervieu, *J. Solid State Chem.* **2006**, *179*, 3849.
[20] C. Michel, N. Nguyen, R. Retoux, B. Raveau, *Eur. J. Solid State Inorg. Chem.* **1988**, *25*, 375.
[21] R. Retoux, C. Michel, M. Hervieu, N. Nguyen, B. Raveau, *Solid State Commun.* **1989**, *69*, 599.
[22] C. Lepoittevin, S. Malo, M. Hervieu, D. Grébille, B. Raveau, *Chem. Mater.* **2004**, *16*, 5731.
[23] *The Chemistry of Extended Defects in Non-Metallic Solids* (Eds.: L. Eyring, M. O'Keeffe), North Holland, Amsterdam, **1970**.
[24] M. Hervieu, C. Michel, M. T. Caldes, A. Q. Pham, B. Raveau, *J. Solid State Chem.* **1993**, *107*, 117.
[25] M. Hervieu, M. T. Caldes, C. Michel, D. Pelloquin, S. Cabrera, B. Raveau, *J. Mater. Chem.* **1996**, *6*, 175.
[26] M. Hervieu, M. T. Caldes, C. Michel, D. Pelloquin, B. Raveau, *J. Solid State Chem.* **1995**, *118*, 357.
[27] M. Hervieu, O. Perez, D. Groult, D. Grebille, H. Leligny, B. Raveau, *J. Solid State Chem.* **1997**, *129*, 2, 214.
[28] O. Perez, H. Leligny, G. Baldinozzi, D. Grebille, M. Hervieu, P. Labbé, D. Groult, H. Graafsma, *Phys. Rev. B* **1997**, *56*, 5662.
[29] M. Allix, O. Perez, D. Pelloquin, M. Hervieu, B. Raveau, *J. Solid State Chem.* **2004**, *177*, 3187.
[30] C. Lepoittevin, S. Malo, O. Pérez, N. Nguyen, A. Maignan, M. Hervieu, *Solid State Sci.* **2006**, *8*, 1294.
[31] P. M. Woodward, *Acta Crystallogr. Sect. A* **1997**, *53*, 32.
[32] G. VanTendeloo, S. Amelinckx, *Acta Crystallogr. Sect. A* **1974**, *30*, 431.
[33] E. O. Wollan, W. C. Koehler, *Phys. Rev.* **1955**, *100*, 545.
[34] N. Kumar, C. N. R. Rao, *J. Solid State Chem.* **1997**, *129*, 363; P. M. Woodward, T. Vogt, D. E. Cox, A Arulraj, C. N. R. Rao, P. Karen, A. K. Cheetham, *Chem. Mater.* **1998**, *10*, 3652.
[35] a) J. B. Goodenough, *Phys. Rev.* **1955**, *100*, 564; b) A. Daoud-Aladine, *Phys. Rev. Lett.* **2002**, *89*, 097205.
[36] C. H. Chen, S. W. Cheong, *Phys. Rev. Lett.* **1996**, *76*, 4042.
[37] A. Barnabe, M. Hervieu, C. Martin, A. Maignan, B. Raveau, *J. Mater. Chem.* **1998**, *8*, 1405.
[38] P. Laffez, G. Van Tendeloo, F. Millange, V. Caignaert, M. Hervieu, B. Raveau, *Mater. Res. Bull.* **1996**, *31*, 905.
[39] P. G. Radaelli, D. E. Cox, M. Marezio, S. W. Cheong, P. E. Schiffer, A. P. Ramirez, *Phys. Rev. Lett.* **1995**, *75*, 4488.
[40] M. R. Ibarra, J. M. de Teresa, J. Blasco, P. A. Algaratel, C. Marquina, J. Garcia, J. Stankiewics, C. Ritter, *Phys. Rev. B* **1997**, *56*, 8252.

[41] K. Liu, X. W. Wu, K. H. Ahr, T. Sulchek, C. L. Chien, J. O. Xiao, *Phys. Rev. B* **1996**, *54*, 3007.
[42] W. Schuddinck, O. Richard, G. Van Tendeloo, F. Millange, M. Hervieu, B. Raveau, *Acta Crystallogr. Sect. A* **1999**, *55*, 704.
[43] M. Hervieu, A. Barnabe, C. Martin, A. Maignan, F. Damay, B. Raveau, *Eur. Phys. J. B* **1999**, *8*, 31.
[44] W. Bao, J. D. Axe, C. H. Chen, S. W. Cheong, *Phys. Rev. B* **1997**, *78*, 543.
[45] H. Chiba, M. Kikuchi, K. Kusaba, H. Muruoka, Y. Syono, *Solid State Commun.* **1996**, *99*, 499.
[46] A. Daoud-Aladine, J. Rodriguez Carvajal, L Pinsard-Gaudart, M. T. Fernandez-Diaz, A. Revcholevschi, *Phys. Rev. Lett.* **2002**, *89*, 097205.
[47] Z. Jirak, C. Martin, M. Hervieu, J. Hejtmànek, *Appl. Phys. A* **2002**, *74*, S1755.
[48] A. Barnabe, A. Maignan, M. Hervieu, F. Damay, C. Martin, B. Raveau, *Appl. Phys. Lett.* **1997**, *71*, 26.
[49] B. Raveau, A. Maignan, C. Martin, M. Hervieu, *J. Solid State Chem.* **1997**, *130*, 162.
[50] T. Kimura, Y Tomioka, Y Tokura, *Phys. Rev. Lett.* **1999**, *83*, 3940.
[51] R. Mahendiran, M. Hervieu, A. Maignan, C. Martin, B. Raveau, *Solid State Commun.* **2000**, *114*, 429.
[52] A. Barnabe, M. Hervieu, C. Martin, A. Maignan, B. Raveau, *J. Mater. Chem.* **1998**, *8*, 1405; F. Damay, C. Martin, A. Maignan, M. Hervieu, B. Raveau, Z. Jirak, G. Andre, F. Bouree, *Chem. Mater.* **1999**, *11*, 536; C. Martin, A. Maignan, F. Damay, M. Hervieu, B. Raveau, Z. Jirak, G. andre, F. Bouree, *J. Magn. Magn. Mater.* **1999**, 202, 11. W. Schuddinck, G. Van Tendeloo, M. Hervieu, *J. Solid State Chem.* **1999**, *148*, 333; R. Mahendiran, M. Hervieu, A. Maignan, C. Martin, B. Raveau, *Solid State Commun.* **2000**, *114*, 429; M. Hervieu, C. Martin, A. Barnabe, A. Maignan, R. Mahendiran, V. Hardy, *Solid State Sci.* **2001**, *3*,391.
[53] C. Martin, A. Maignan, M. Hervieu, B. Raveau, J. Hejtmanek, *Eur. Phys. J. B* **2000**, *16*, 469.
[54] C. Martin, A. Maignan, M. Hervieu, B. Raveau, J. Hejtmanek, *Phys. Rev. B* **2001**, *63*, 100406(R).
[55] A. Maignan, C. Martin, C. Autret, M. Hervieu, B. Raveau, J. Hejtmanek, *J. Mater. Chem.* **2002**, *12*, 1806.
[56] A. Maignan, C. Martin, C. Autret, M. Hervieu, B. Raveau, *J. Appl. Phys.* **2002**, *91*, 4267.
[57] M. Miclau, J. Hejtmanek, R. Retoux, K. Knizek, Z. Jirak, R. Fresard, A. Maignan, S. Hebert, M. Hervieu, C. Martin, *Chem. Mater.* **2007**, *19*, 4243.

Published online: December 14, 2007

